



Transport analysis in deformable porous media through integral transforms

Alessandra Bonazzi¹ | Birendra Jha² | Felipe P. J. de Barros¹

¹ Sonny Astani Department of Civil and Environmental Engineering, University of Southern California, Los Angeles, California

² Mork Family Department of Chemical Engineering and Materials Science, University of Southern California, Los Angeles, California

Correspondence

Felipe P. J. de Barros, Sonny Astani Department of Civil and Environmental Engineering, University of Southern California, Los Angeles, CA 90089-2531.
Email: fbarros@usc.edu

Funding information

National Science Foundation, Grant/Award Number: 1654009

Abstract

Geomechanical deformation can alter the flow field that impacts solute mass fluxes. Despite its importance, the effects of the coupling between geomechanical deformation and the flow field on solute transport behavior are not fully known. In this paper, we study the impact of this coupling on the solute concentration distribution. The concentration field is semianalytically derived by making use of the generalized integral transform technique. We apply the semi-analytical solution to two uniaxial consolidation problems, the classical Terzaghi's problem with a constant load and the case of periodic loading of a porous deformable layer. Our results indicate that geomechanical parameters, such as the Skempton's coefficient and the soil compressibility, can affect the peak concentration as well as the spatial moments of solute plume. In case of periodic loading, we show that the frequency of loading also plays a key role in regulating the temporal dynamics of the concentration field.

KEYWORDS

geomechanics, integral transforms, poroelasticity, solute transport, Terzaghi's problem

1 | INTRODUCTION

The coupling between geomechanical deformation and fluid flow is of critical importance in a variety of applications in hydrogeology and reservoir engineering. In particular, the most severe environmental impacts of these applications are land subsidence and earthquakes caused by extraction of water and hydrocarbons.^{1–5} Subsidence is commonly associated with groundwater extraction in unconsolidated alluvial systems, where the extraction causes compaction.³ Seismicity is associated with movement along basement faults that are activated due to stresses induced by fluid extraction.² It is also acknowledged that earthquakes can be induced by the injection of fluid into the subsurface aquifers. Several studies^{6,7} have demonstrated the geomechanical effects of wastewater disposal on seismicity. Geomechanical effects of CO₂ storage in deep saline aquifers include seismicity as well as leakage of brine into fresh groundwater reservoirs.^{8–10} The mathematical formulation of ground deformation problems, including injection and production-induced seismicity, is provided by Biot's poroelasticity theory.¹¹

Although the characterization of the impact of geomechanical deformations on flow has been thoroughly investigated,^{4,12–17} its consequences on solute transport in aquifers have not received a proportionate amount of attention despite its importance. It is well known that seismicity can lead to water-level oscillations,¹⁸ increased turbidity,¹⁹ and possible water release from storage caused by an increase in pore pressure and changes in permeability due to fracturing or consolidation.²⁰ The creation of new fractures could increase the aquifer vulnerability to surface contamination, and the change in preferential flow paths could have severe consequences such as wells capturing younger waters,²¹ which could be a serious issue, for instance, in indirect potable reuse applications. The water-level decline associated with subsidence impacts hydrological fluxes and can lead to the overall deterioration of water quality due to a higher

probability of seawater or wastewater infiltration in the aquifer,²¹ a possible release from storage of water with different chemical composition²² and an increased vulnerability to anthropogenic pollution sources.²¹ The consolidation process that accompanies subsidence can potentially induce mobilization of contaminants,²³ as in case of consolidation-induced transport in landfills.²⁴

Groundwater vulnerability related to geomechanical deformations has been evaluated through numerical modeling (deterministic and stochastic), GIS (Geographic Information System) tools, and well capture zone analysis (employing both field data analysis and numerical models).²⁵ Although many numerical models focus on the consolidation and fracturing induced by water extraction,^{26–28} a few works^{23, 29} investigated the effects of consolidation-induced flow on solute transport, which is of relevance to landfill consolidation. A reduction in the breakthrough time of contaminant across a plane was reported²⁹ due to consolidation and found advection to have a lesser impact on the contaminant transit time than variations in geometry and porosity. Strong coupling between the fluid velocity field and the contaminant concentration profile was found to be necessary for the advective transport to be significant,²⁴ and the reduction in the breakthrough time is dependent on the compressibility of the porous medium. In agreement to that,³⁰ it is concluded that in order to retard contaminant transport, the best strategy is to reduce soil compressibility and increase sorption. It was also found³¹ that the contribution of spatial variability in porosity to contaminant transport is negligible. Recently, the impact of poroelasticity on solute transport was numerically investigated for fluids of different compressibility and viscosity, especially in the presence of viscous instability,³² and it was found that, analogously to landfills, more compressible porous media lead to earlier solute breakthrough times.

Most numerical models of coupled geomechanics and transport focus on one-dimensional (1D) domains. This simplification allows the derivation of analytical and semianalytical solutions for the transport problem described by the advection-dispersion equation (ADE) for different sets of initial and boundary conditions. For example, Li and Cleall³³ derived the analytical solution for the concentration field for five different scenarios in a double-layered porous medium, presenting an application on consolidation-induced advective transport of trichloropropane and analyzing the solute flux in time to quantify the contribution of advection with respect to diffusion-only models;³⁴ Xie et al.³⁴ developed an analytical model for the transport of volatile organic compounds in a landfill due to leakage, neglecting consolidation. Despite these efforts,^{33, 34} most of the available analytical solutions for the ADE do not deal with the contribution of deformations to flow, thus missing the opportunity of investigating the functional relationship between geomechanical parameters and contaminant transport characterisation. For such reasons, there is still need to improve our fundamental understanding of the impact of geomechanical deformation on transport.

In this work, we develop an integral transform-based semianalytical solution for the coupled flow, transport, and deformation problem in a 1D domain of finite length. The solution is based on the hybrid analytical-numeric methodology known as the generalized integral transform technique.^{35–37} The solution is applied to two classic cases: a layer subjected to consolidation and one where an harmonic load is applied. In the first case, our work extends the solution of the classical Terzaghi's problem to include transport of a passive tracer.^{38, 39} Terzaghi's problem is based on the consolidation of an uniaxially constrained soil column and its applicability ranges from subsidence¹⁴ to landfills to other phenomena that can be ascribed to a 1D consolidation process.⁴⁰ In the second case, our solution investigates the transport phenomenon occurring when the flow field is the result of a periodic loading,^{39, 41} a model that has been applied to the problem of storm and tidal wave-induced pore pressure^{42–44} and to study the effect of seismic waves.⁴⁵ The developed solution for solute transport will allow us to investigate how geomechanical deformation impacts transport quantities both at the local (e.g., solute resident concentration distribution in space and time) and at the global (e.g., spatial moments of the plume) scales. Our solution provides new insights on the functional relationships between these transport quantities and the geomechanical parameters. These relationships, which have traditionally been neglected, can improve our understanding of the role of poroelasticity in solute transport and enable discovery of new methods to control the response of engineered subsurface systems.

2 | PHYSICAL FORMULATION

2.1 | Coupled flow and geomechanics

2.1.1 | Case 1: Terzaghi's problem

Terzaghi's problem consists of an uniaxial consolidation test under drained conditions, meaning that the soil/rock column is constrained on all sides except the top boundary, where water is allowed to drain out of the domain freely,^{17, 39} as depicted

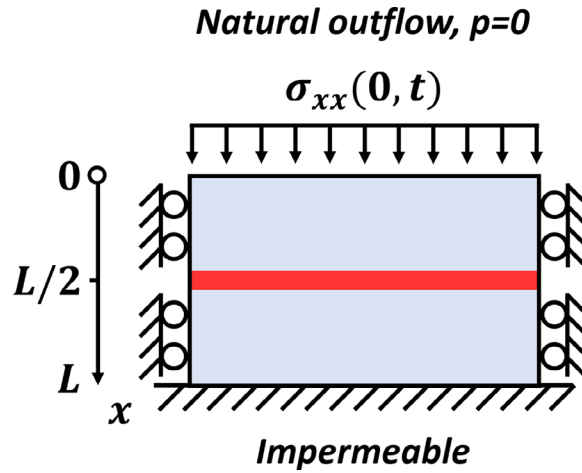


FIGURE 1 Physical domain for cases 1 and 2. The left and right boundaries reflect the zero normal displacement condition, and the bottom boundary is fixed. The red line corresponds to the initial position of the instantaneously released inert tracer

in Figure 1. We consider a water-saturated 1D finite soil/rock layer of dimension L along the coordinate direction x where $0 \leq x \leq L$. A sudden stress $-\sigma_0$ (negative implies compression) is applied on the top of the layer at time $t = 0$, which remains constant in time. The excess pore pressure p (above hydrostatic) dissipates over time and space according to the following governing equation (see [39] for details):

$$\frac{\partial p}{\partial t} = C \frac{\partial^2 p}{\partial x^2}, \quad (1)$$

where C is the consolidation coefficient. At $t = 0$, the initial condition for Equation (1) is given by the undrained pressure

$$p(x, 0) = p_0 = \gamma \sigma_0, \quad (2)$$

where γ is the loading efficiency and is a function of the undrained Poisson's ratio ν_u and Skempton's coefficient S_k . Neglecting body forces such as gravity, the quasi-static mechanical equilibrium equation in the x -direction is

$$\frac{\partial \sigma_{xx}}{\partial x} = 0. \quad (3)$$

Assuming the x -axis as positive downward (see Figure 1), the boundary conditions for the stress σ_{xx} , displacement δ_x and pressure p , are:

$$\sigma_{xx}(0, t) = -\sigma_0; \quad (4)$$

$$\delta_x(L, t) = 0; \quad (5)$$

$$\left. \frac{\partial p}{\partial x} \right|_{x=L} = 0; \quad (6)$$

$$p(0, t) = 0. \quad (7)$$

The solid skeleton deforms in response to a change in the effective stress, which is defined as $\sigma' = \sigma + bp$, where b is the Biot coefficient that can be expressed in terms of the specific storage S , ν_u , and S_k . Assuming that the material behavior is linear elastic and isotropic (or transversely isotropic with the bedding plane perpendicular to the load axis and the flow vector), the stress-strain relation is $\sigma'_v = K_v \varepsilon_v$, where σ'_v is the effective volumetric stress, ε_v is the volumetric strain, and K_v is the drained uniaxial modulus that can be obtained from the uniaxial compressibility $c_m = b/K_v$. For the uniaxial conditions considered here, $\sigma'_v = \sigma'_{xx}$ and $\varepsilon_v = d\delta_x/dx$. The theory of linear poroelasticity shows that for this particular 1D case with a constant applied stress, the total stress in the domain is a constant, $-\sigma_0$, and the pore pressure is decoupled

from the stress field. The effective stress and the displacement change with time due to the fluid-to-solid coupling. The analytical solution for the excess pressure field subject to boundary and initial conditions given in Equations (2)–(13)³⁹ is

$$p(x, t) = \frac{4\gamma\sigma_0}{\pi} \sum_{m=0}^{\infty} \frac{1}{2m+1} \exp\left[\frac{-(2m+1)^2\pi^2 Ct}{4L^2}\right] \sin\left[\frac{(2m+1)\pi x}{2L}\right]. \quad (8)$$

As time increases, the excess pressure decreases, the load is transferred from the pore fluid (water) to the solid skeleton, and the specimen consolidates.

2.1.2 | Case 2: Periodic load on a finite layer

This case considers a harmonic load applied on top of a finite thickness layer as reported in Refs. [39] and [41]. The periodic load can represent dynamic stress transfer from earthquakes, tides, or seasonal water-level variations above an aquifer. Analogously to Terzaghi's problem, we consider a 1D saturated soil/rock layer of thickness L (see Figure 1). The governing equation for the excess pressure in this case is given by:

$$\frac{\partial p}{\partial t} = C \frac{\partial^2 p}{\partial x^2} - \gamma \frac{d\sigma_{xx}}{dt}, \quad (9)$$

where the rate of change of total vertical stress on the right-hand side provides the solid-to-fluid coupling that was missing in the classical Terzaghi problem. The periodic load boundary condition is:

$$\sigma_{xx}(0, t) = -\sigma_0 e^{i\omega t}, \quad (10)$$

in which $\iota = \sqrt{-1}$ and ω is the period of the harmonic load variation. Because of Equation (3), $\sigma_{xx}(x, t) = \sigma_{xx}(0, t)$. The boundary conditions for pressure p and displacement δ_x are:

$$\delta_x(0, t) = 0; \quad (11)$$

$$\left. \frac{\partial p}{\partial x} \right|_{x=L} = 0; \quad (12)$$

$$p(0, t) = 0. \quad (13)$$

The solution will have form:^{39, 41}

$$p(x, t) = \Re\{\tilde{p}(x)e^{i\omega t}\}, \quad (14)$$

where $\Re\{\cdot\}$ corresponds to the real part of the solution and the complex amplitude $\tilde{p}(x)$ is expressed as:

$$\tilde{p}(x) = \gamma\sigma_0 \left[1 + \tanh\left(L\sqrt{\frac{i\omega}{C}}\right) \sinh\left(x\sqrt{\frac{i\omega}{C}}\right) - \cosh\left(x\sqrt{\frac{i\omega}{C}}\right) \right]. \quad (15)$$

The pressure field will thus be physically represented by the real part of $\tilde{p}(x)e^{i\omega t}$, see Equation (14) and details in Ref. [41].

2.2 | Solute transport

We consider transport of a fully dissolved ideal tracer. The tracer is instantaneously injected into the soil sample and the spatiotemporal evolution of the concentration field $c(x, t)$ is assumed to be governed by the ADE:

$$\frac{\partial(\phi(x, t)c(x, t))}{\partial t} + \frac{\partial(q(x, t)c(x, t))}{\partial x} = \frac{\partial}{\partial x} \left[\phi(x, t)D(x, t) \frac{\partial c(x, t)}{\partial x} \right], \quad (16)$$

where $\phi(x, t)$ is the porosity, $q(x, t)$ is the specific discharge, and $D(x, t)$ is the hydrodynamic dispersion coefficient. From the pressure field for cases 1 and 2 (see Equations 8 and 14), we can compute the specific discharge $q(x, t)$ according to Darcy's equation:

$$q(x, t) = -\frac{k}{\mu} \frac{\partial p(x, t)}{\partial x}, \quad (17)$$

where k is the permeability and μ is the fluid's absolute viscosity. Both k and μ are considered to be constants. The boundary and initial conditions for the transport problem are as follows:

$$\left. \frac{\partial c}{\partial x} \right|_{x=0} = 0; \quad (18)$$

$$\left. \frac{\partial c}{\partial x} \right|_{x=L} = 0; \quad (19)$$

$$c(x, 0) = f(x). \quad (20)$$

Note that $f(x)$ can assume any functional shape. Moreover, the ADE presented in Equation (16) accounts for coefficients that vary in space and time. This is an outcome of the flow conditions described in cases 1 and 2.

3 | SOLUTION METHODOLOGY FOR TRANSPORT

To solve Equations (16)–(20), we will make use of the generalized integral transform technique (GITT).^{35, 37} This technique has been employed to study scalar dynamics in environmental flows.^{36, 46, 47} We apply the GITT for the first time to study solute transport in coupled geomechanics and fluid flow problems. As summarized in Ref. [35], the GITT is based on the following steps:

1. development of the integral transform pair and choice of the associated eigenvalue problem;⁴⁸
2. application of the integral transform to the ADE to obtain a system of coupled ordinary differential equations (ODEs);
3. numerical solution of the system of coupled ODEs for the transformed potentials; and
4. application of the inversion formula to compute the concentration field.

For our study, we consider porosity ϕ as a constant based on the arguments described in Appendix A. We thus rewrite Equation (16) as follows:

$$\begin{aligned} & \frac{\partial c(x, t)}{\partial t} + c(x, t) \frac{\partial u(x, t)}{\partial x} + u(x, t) \frac{\partial c(x, t)}{\partial x} \\ & = D_0 \frac{\partial^2 c(x, t)}{\partial^2 x} + \check{D}(x, t) \frac{\partial^2 c(x, t)}{\partial^2 x} + \frac{\partial c(x, t)}{\partial x} \frac{\partial \check{D}(x, t)}{\partial x}, \end{aligned} \quad (21)$$

where we decomposed the dispersion coefficient as $D(x, t) = D_0 + \check{D}(x, t)$ and $u(x, t) = q(x, t)/\phi$ represents the interstitial velocity. D_0 is the constant molecular diffusion coefficient, and $\check{D}(x, t)$ is the mechanical dispersion coefficient calculated as $\check{D}(x, t) = \alpha |u(x, t)|$, where α is the constant dispersivity.⁴⁹

The integral transform and its inverse are defined as:

$$\hat{c}_i(t) = \int_0^L \Psi_i(x) c(x, t) dx; \quad (22)$$

$$c(x, t) = \sum_{i=0}^{\infty} \Psi_i(x) \hat{c}_i(t); \quad (23)$$

where $\hat{c}_i(t)$ is the transformed scalar and

$$\Psi_i(x) = \frac{1}{\sqrt{N_i}} \Psi_i(x), \quad (24)$$

where $\Psi_i(x)$ and N_i denote the i th eigenfunction and norm originating from the eigenvalue problem given below:

$$\frac{d^2\Psi_i(x)}{d^2x} = \lambda_i^2\Psi_i(x), \quad (25)$$

$$\left. \frac{d\Psi_i(x)}{dx} \right|_{x=0} = 0, \quad (26)$$

$$\left. \frac{d\Psi_i(x)}{dx} \right|_{x=L} = 0, \quad (27)$$

where $\lambda_i^2 = \zeta_i^2/D_0$ and λ_i denote the eigenvalues. The solution for $\Psi_i(x)$ and λ_i are given by:⁵⁰

$$\Psi_i(x) = \cos(\lambda_i x); \quad (28)$$

$$\lambda_i = \frac{i\pi}{L}, \quad i = 0, 1, \dots, \infty, \quad (29)$$

with norm N_i :

$$N_i = \begin{cases} L & \text{if } i = 0 \\ \frac{L}{2} & \text{if } i \neq 0. \end{cases} \quad (30)$$

Our next step consists of multiplying Equations (21) and (20) by $\Psi_i(x)$ and integrating over the domain $x \in [0, L]$. Applying the boundary conditions and solving all the integral terms (see Appendix B for details), we obtain the system of coupled ODEs

$$\frac{d\hat{c}_i(t)}{dt} = - \sum_{j=0}^N \hat{c}_j(t)U_{ij}(t) - \sum_{j=0}^N \hat{c}_j(t)A_{ij}(t) - \zeta^2\hat{c}_i(t) - \sum_{j=0}^N \hat{c}_j(t)B_{ij}(t), \quad (31)$$

$$\hat{c}_i(0) = \int_0^L \tilde{\Psi}_i(x)f(x) dx, \quad (32)$$

in which the temporally variable coefficients $U_{ij}(t)$, $A_{ij}(t)$, and $B_{ij}(t)$ are defined as

$$U_{ij}(t) = \int_0^L \tilde{\Psi}_i(x) \frac{\partial u(x, t)}{\partial x} \tilde{\Psi}_j(x) dx, \quad (33)$$

$$A_{ij}(t) = \int_0^L u(x, t) \tilde{\Psi}_i(x) \frac{d\tilde{\Psi}_j(x)}{dx} dx, \quad (34)$$

$$B_{ij}(t) = \int_0^L \check{D}(x, t) \frac{d\tilde{\Psi}_i}{dx} \frac{d\tilde{\Psi}_j}{dx} dx. \quad (35)$$

Note that Equations (31) and (32) form a system of N coupled ODEs and the corresponding N initial conditions, where N is the number of eigenvalues. The value of N is chosen to be large enough to reach convergence of the solution. The system of coupled ODEs is numerically solved using the *Mathematica*'s⁵¹ built-in function `NDSolve` to find the unknowns $\hat{c}_i(t)$ for $i = 0, 1, 2, \dots, N$. Once the solution for $\hat{c}_i(t)$ is obtained, we invoke the inversion formula (Equation 23) to compute $c(x, t)$. For completeness, we include the system of coupled ODEs for the case with variable porosity in Appendix C.

Due to the GITT's computationally hybrid features,³⁷ we can derive semianalytical expressions for the solute plume's spatial moments. Making use of Equation (23), the zeroth moment (i.e., mass) is calculated as:

$$\mu^{(0)}(t) = \int_0^L \phi c(x, t) dx = \phi \sum_{i=0}^N \hat{c}_i(t) \int_0^L \tilde{\Psi}_i(x) dx. \quad (36)$$

Inserting Equation (28) into Equation (36), we get:

$$\mu^{(0)}(t) = \phi \left[\hat{c}_0(t)L + \sum_{i=1}^N \hat{c}_i(t) \frac{L \sin(\pi i)}{\pi i} \right]. \quad (37)$$

The first moment (i.e., location of the plume's centroid) is similarly obtained as:

$$\mu^{(1)}(t) = \frac{1}{\mu^{(0)}(t)} \int_0^L \phi x c(x, t) dx = \frac{1}{\mu^{(0)}(t)} \phi \sum_{i=0}^N \hat{c}_i(t) \int_0^L x \Psi_i(x) dx. \quad (38)$$

Utilizing Equations (28) and (37), the first moment can be rewritten as:

$$\mu^{(1)}(t) = \frac{\hat{c}_0(t) \frac{L^2}{2} + \sum_{i=1}^N \hat{c}_i(t) \frac{L^2 [\pi i \sin(\pi i) + \cos(\pi i) - 1]}{\pi^2 i^2}}{\hat{c}_0(t)L + \sum_{i=1}^N \hat{c}_i(t) \frac{L \sin(\pi i)}{\pi i}}. \quad (39)$$

The second noncentral moment is given by:

$$\mu^{(2)}(t) = \frac{1}{\mu^{(0)}(t)} \int_0^L \phi x^2 c(x, t) dx = \frac{\sum_{i=0}^N \hat{c}_i(t) \int_0^L x^2 \Psi_i(x) dx}{\sum_{i=0}^N \hat{c}_i(t) \int_0^L \Psi_i(x) dx}. \quad (40)$$

Substituting Equation (28) and carrying out the integration in Equation (40), we have:

$$\mu^{(2)}(t) = \frac{\hat{c}_0(t) \frac{L^3}{3} + \sum_{i=1}^N \hat{c}_i(t) \frac{L^3 ((\pi^2 i^2 - 2) \sin(\pi i) + 2\pi i \cos(\pi i))}{\pi^3 i^3}}{\hat{c}_0(t)L + \sum_{i=1}^N \hat{c}_i(t) \frac{L \sin(\pi i)}{\pi i}}. \quad (41)$$

Finally the second central moment (i.e., spreading with respect to the plume's centroid position) is given by:

$$\mu_c^{(2)}(t) = \mu^{(2)}(t) - \mu^{(1)}(t)\mu^{(1)}(t), \quad (42)$$

where $\mu^{(1)}(t)$ and $\mu^{(2)}(t)$ are provided in Equations (39) and (41).

4 | ILLUSTRATION

In this section, we computationally implement the semianalytical solution to study transport for the flow configurations in cases 1 and 2 described in Section 2 with the input parameters reported in Table 1. The considered fluid is water, while the parameters characterizing the porous media have been chosen to resemble an aquifer.^{16, 39} Without loss of generality, for all computational results, we assume the following Gaussian form for the initial condition in Equation (20):

$$f(x) = \frac{1}{\sqrt{2\pi}\sigma_c} e^{-\frac{(x-\mu_c)^2}{2\sigma_c^2}}, \quad (43)$$

where $\mu_c = L/2$ and $\sigma_c = 0.4$. All results are reported in dimensionless form.

TABLE 1 Input parameters used in the simulations

Parameter	Symbol	Value	Unit	Calculated as
Fluid compressibility	c_f	4.55×10^{-10}	Pa^{-1}	–
Molecular diffusion	D_0	10^{-9}	m^2/s	–
Gravity	g	9.81	m/s^2	–
Hydraulic conductivity	K_h	10^{-5}	m/s	–
Length of the domain	L	10	m	–
Skempton's coefficient	S_k	0.7	–	–
Dispersivity	α	0.1	m	–
Porosity	ϕ	0.2	–	–
Fluid viscosity	μ	10^{-3}	$\text{Pa} \times \text{s}$	–
Undrained Poisson's ratio	ν_u	0.4	–	–
Fluid density	ρ_f	10^3	kg/m^3	–
Applied load	σ_0	5.5×10^5	Pa	–
Soil compressibility	c_m	6.12×10^{-8}	Pa^{-1}	¹⁶
Consolidation coefficient	C	1.66×10^{-2}	m^2/s	$k/(\mu S)$
Permeability	k	10^{-12}	m^2	$(K_h \mu)/(g \rho_f)$
Specific storage	S	4.55×10^{-10}	Pa^{-1}	$\phi c_f + c_m$
Loading efficiency	γ	0.54	–	$(S_k(1 + \nu_u))/(3(1 - \nu_u))$

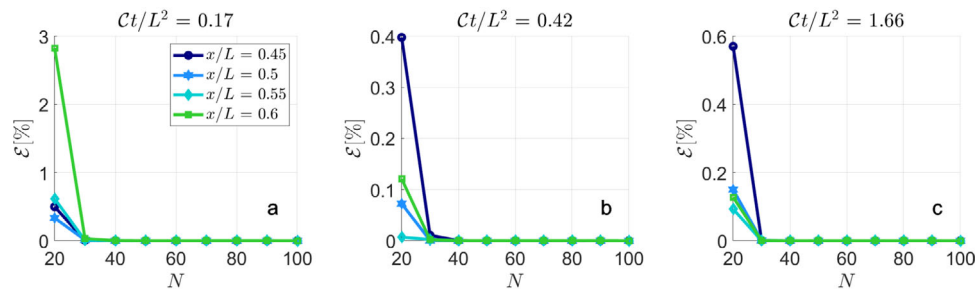


FIGURE 2 Convergence analysis at different dimensionless times Ct/L^2 and locations x/L . Error estimates provided by percentage error for increasing number of eigenvalues N according to Equation (44)

4.1 | Results for case 1

4.1.1 | Verification with numerical solution and convergence analysis

We start by performing a convergence analysis on the GITT solution to determine the number of eigenvalues N needed to compute Equation (31). We analyzed the output of concentration for increasing N at three different times in four locations in the domain. The error was calculated at every considered location x^* and time t^* as:

$$\mathcal{E}(n) = \left| \frac{c(x^*, t^*) \Big|_{N=n} - c(x^*, t^*) \Big|_{N=100}}{c(x^*, t^*) \Big|_{N=100}} \right| \times 100. \quad (44)$$

The results depicted in Figure 2 show that the solution converges for N approximately equal to 40. As expected, the larger errors are observed for lower values of N at early times (compare Figure 2A with Figure 2B-C). In all cases, the results show that the solution converges for $N \gtrsim 35$.

In Figure 3, we verify our semianalytical results against a fully numerical solution for Equation (21) subject to the boundary and initial conditions provided in Equations (18)–(20) and (43). The numerical solution for the ADE is based on *Mathematica*'s built-in function `NDSolve`. The numerical PDE (partial differential equation) solver `NDSolve` uses the

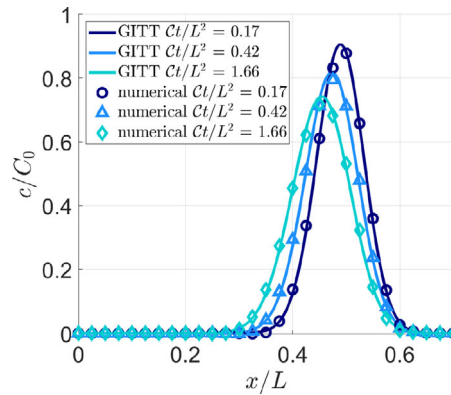


FIGURE 3 Verification of the GITT results against a fully numerical solution at different dimensionless times

method of lines in conjunction with the finite differences method. The concentration $c(x, t)$ has been normalized using the peak concentration at $t = 0$, defined as C_0 . As shown in Figure 3, our integral-transform solution is in good agreement with the numerical result. The shape of the solution suggests that diffusion plays an important role in the transport process. We observe lower concentration gradients at later times. This is aligned with the experimental observations in Ref. [52] where a slower loading rate experiment, which allowed additional time for diffusion, resulted in lower concentration gradients within the slurry column.

4.1.2 | Computational results

Next we investigate how the key metrics characterizing the concentration field are impacted by the soil compressibility c_m , porosity ϕ , and Skempton's coefficient S_k . The analysis was performed by increasing and decreasing the selected parameters by a factor of 20%, denoted as ϵ . With the exception of the varying parameter, all the other quantities remained the same for all simulations. For the Terzaghi's problem, the solute plume moves until the excess pore pressure is completely dissipated; after then the only contribution to transport is given by molecular diffusion. This is clearly visible in Figure 4, where both first and second central spatial moments do not change for $Ct/L^2 \gtrsim 12$.

The results obtained for the first moment $\mu^{(1)}$ (Figure 4A-C) show that variations in c_m and S_k have similar effects on the spatial moments, leading to the center of mass moving faster and further if they increase, and slower otherwise, while an increase in ϕ causes the flow field to slow down and thus obstacles the movement of the center of mass. Moreover, the response of the solute plume due to variations in c_m and S_k seems almost symmetrical, i.e., increasing or decreasing the parameters by the same factor cause $\mu^{(1)}$ to increase or decrease in a similar way. On the other hand, increasing ϕ has a lesser impact on $\mu^{(1)}$ than decreasing it, as visible in Figure 4B where the red area is smaller than the yellow one. Analogous results are obtained for the second central moments $\mu_c^{(2)}$, meaning that variations that cause an increase in $\mu^{(1)}$ lead to an increase in $\mu_c^{(2)}$ as well, and vice versa. These results can be explained by the expression for the velocity field $u(x, t)$ obtained from Equations (8) and (17). In fact, an increase in c_m will result in an increase in specific storage S and, consequently, a decrease in the consolidation coefficient C (see Table 1). This will slow down the dissipation of the excess pore pressure, thus allowing the solute plume to travel more before stopping completely. A similar effect is caused by an increase in S_k , which will lead to an increase in the loading efficiency γ that will, in turn, increase the absolute module of the velocity field, allowing the solute plume to travel faster. Note that from the relation $u(x, t) = q(x, t)/\phi$, it is possible to understand why an increase in ϕ leads to effects that are opposite compared to the effects of increasing c_m or S_k .

A quantity of interest in risk assessment is the solute plume's peak concentration c_{peak} , which accounts for the maximum level of contamination. As visible in Figure 5, the sensitivity of the peak concentration to variations in the selected parameters depends on the time of interest: at early times, especially for variations in c_m , c_{peak} is not affected by such variations, while at late times we can observe a nearly 10% change in the peak concentration. Another interesting observation is that the effect of uncertainty in geomechanical parameter values, especially c_m , is not symmetric around the base case $\epsilon = 0$. In other words, if the base case is overestimating the true value of c_m , then the effect of this error will disappear with time faster than if the base case were underestimating the true value of c_m . This analysis shows that geomechanical parameters can significantly impact risk assessment in contaminated sites.

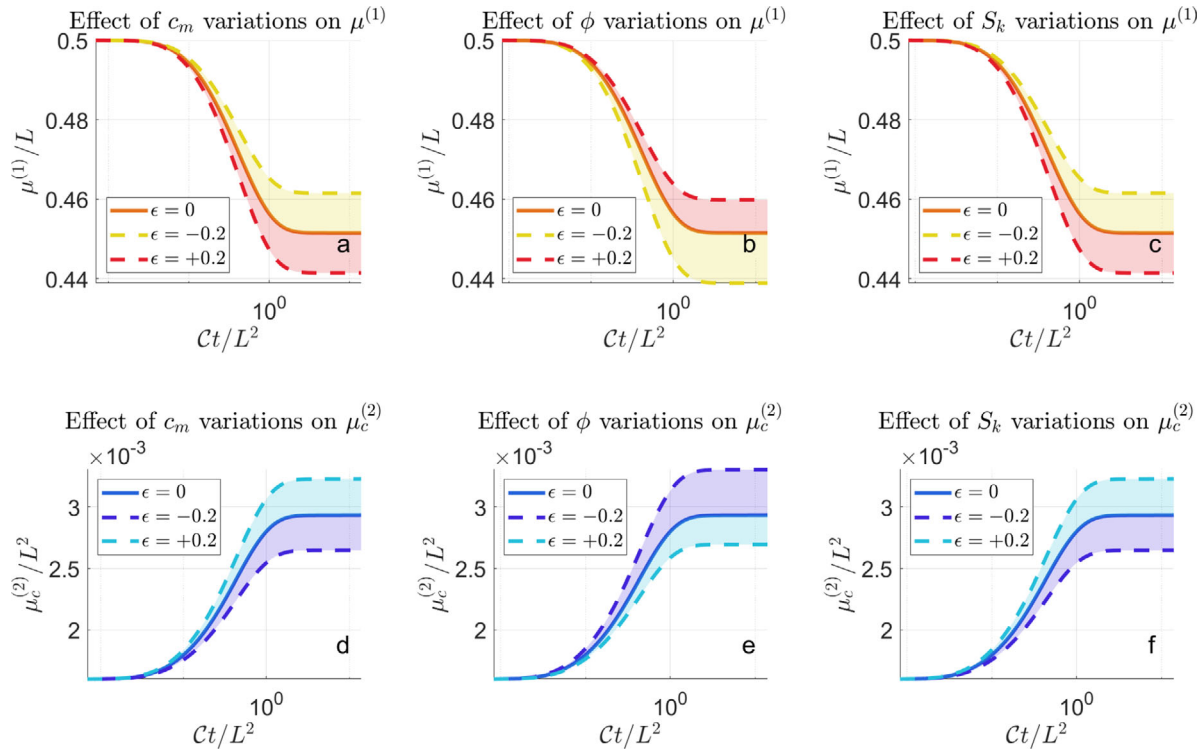


FIGURE 4 Temporal evolution of the solute plume's spatial moments. Results shown for different values of the vertical medium compressibility c_m , porosity ϕ , and Skempton coefficient S_k

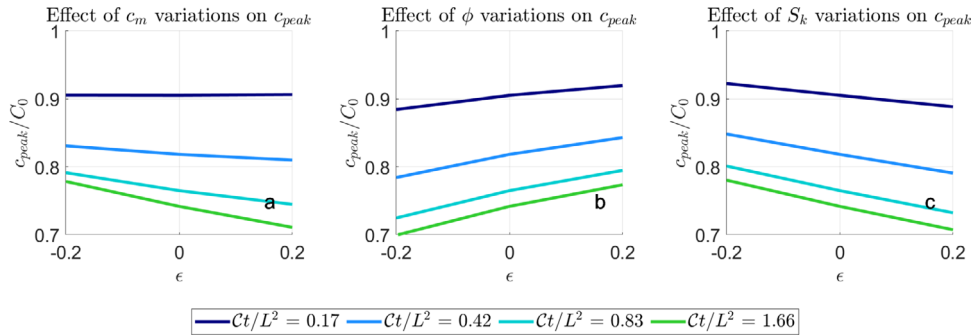


FIGURE 5 Effect of $\pm 20\%$ variations ϵ in c_m , ϕ , and S_k on the solute plume's peak concentration c_{peak} at different times

4.2 | Results for case 2

4.2.1 | Constant and variable D and verification with numerical solution

Now we present transport predictions for the case of a periodic load characterized by a frequency ω . Similar to previous works on transport in temporally fluctuating flows,⁵³ we will illustrate our results with a constant mechanical dispersion coefficient $\check{D} = \alpha|\bar{u}|$ with α denoting the dispersivity (see Table 1) and \bar{u} computed as:

$$\bar{u} = \frac{2\omega}{L} \int_0^{1/2\omega} \int_0^L u(x, t) dx dt, \quad (45)$$

where the temporal average is taken over a semiperiod.

To examine the consequences of the constant \check{D} assumption, we compute the concentration with a spatially and temporally variable \check{D} . We compare the results for the concentration field obtained for a constant and variable mechanical

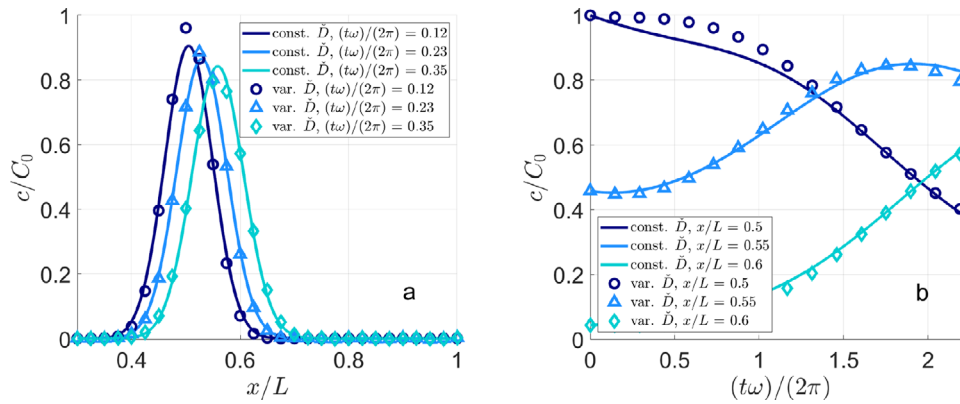


FIGURE 6 Values of $c(x, t)/C_0$ in space at three different times (left) and values of $c(x, t)/C_0$ in time at three different locations ($x/L = 0.5, 0.55,$ and 0.6) (right) for constant and variable \check{D}

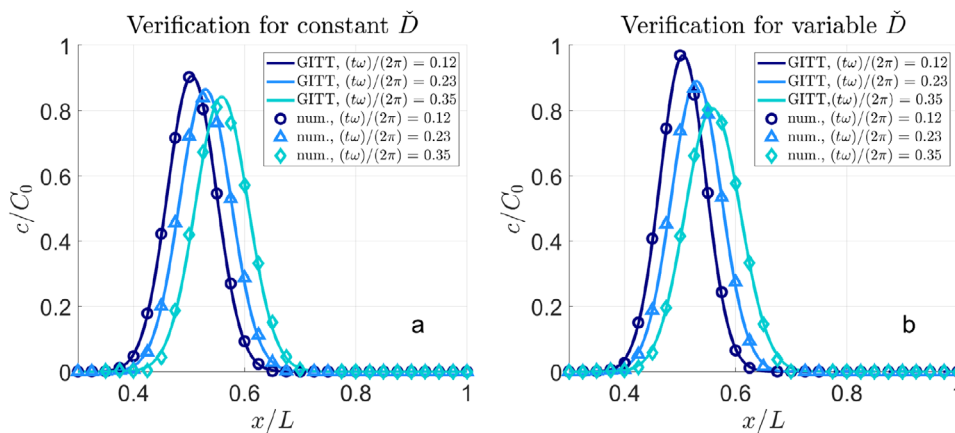


FIGURE 7 Verification of the GITT solution against a fully numerical solution for constant (left) and variable (right) \check{D}

dispersion (Figure 6). As visible in Figures 6A and 6B, some differences are noted between these two cases; however, the effects of variable dispersion are not significant for the range of parameters explored in this study. Our results show that the constant \check{D} assumption allows to capture the general transport behavior of the plume. For completeness, Figure 7 includes the comparison between the GITT solution and a fully numerical solution obtained by *Mathematica's* built-in differential equation solver *NDSolve*.⁵¹ As observed in Figure 7, both solutions are in good agreement for constant (Figure 7A) and variable (Figure 7B) dispersion.

4.2.2 | Computational results

Next, we consider the computation of the solution for $\check{D} = 2.0 \times 10^{-6} \text{ m}^2/\text{s}$ (calculated using Equation 45 and $\omega = 7.3 \times 10^{-5} \text{ s}^{-1}$). Figure 8 shows the oscillatory behavior of the solute plume throughout the domain, while Figure 9 illustrates the concentration signal versus time at two locations ($x/L = 0.5$ and $x/L = 0.6$) for different values of ω . The selected values of ω are based on $\pm 10\%$ perturbation on the reference $\omega = 7.3 \times 10^{-5} \text{ s}^{-1}$. It is observed that ω has a significant impact on the concentration signal. Furthermore, the results in Figure 9A show that the changes in the angular frequency mainly affects the concentration values at early times and becomes negligible after a few periods. On the other hand, Figure 9B shows that the effects of ω on $c(x, t)$ are prolonged in time if we monitor the concentration breakthrough curve at a different position in space (compared with Figure 9A). The results in Figures 8 and 9 suggest the importance of periodic loading in controlling the magnitude of the concentration.

Finally, Figure 10 shows the effects of ω on the first and second central spatial moments of the solute plume. As expected, both spatial moments oscillate in time. Variations in ω do not affect the first moment, while it seems that the spread of the

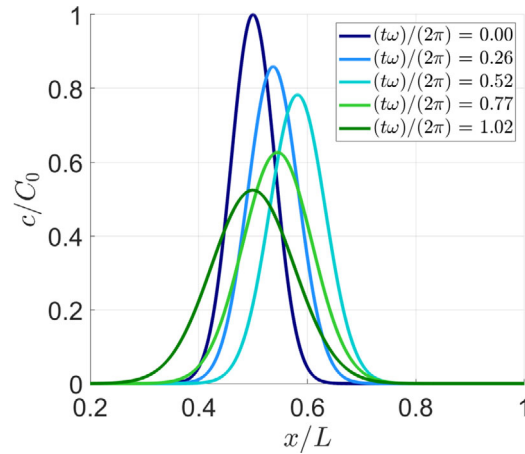


FIGURE 8 Spatial distribution of the concentration at different times. All results displayed in dimensionless form

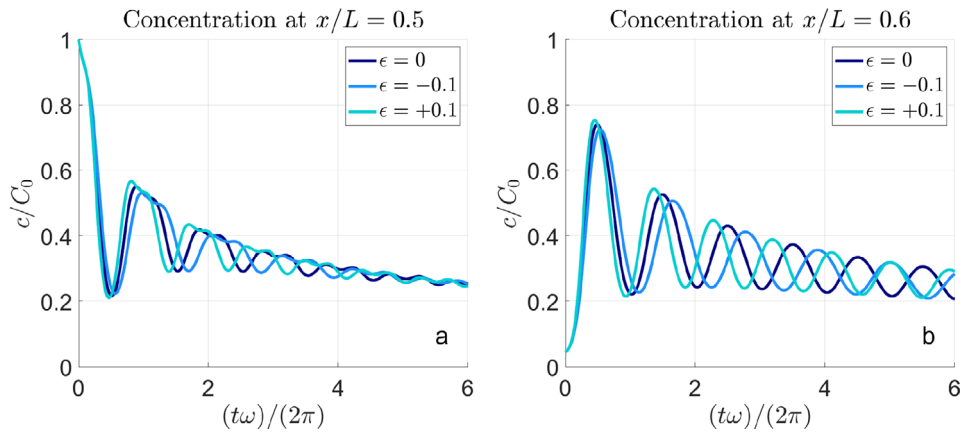


FIGURE 9 Temporal evolution of the solute concentration at two different locations ($x/L = 0.5$ and $x/L = 0.6$) for different ω values. All results displayed in dimensionless form

solute plume is enhanced by lower angular frequencies, as suggested by the higher values of the second central moment for a decrease in ω .

5 | CLOSING REMARKS

This study develops an integral transform-based solution to predict the concentration field in a deformable porous medium. We show how the concentration field is affected by the flow-geomechanics coupling effect for two classical problems: Terzaghi's problem and a porous medium undergoing a periodic load. In both cases, the geomechanical deformation induces a spatially and temporally variably Darcy-scale velocity field. As a consequence, the ADE is characterized by coefficients that vary in both space and time that renders challenging to develop a fully analytical solution for the concentration field. To overcome this difficulty, we propose to solve the ADE with a hybrid numerical-analytical approach known as the GITT.³⁵ The results obtained with our proposed methodology showed good agreement with the results obtained from purely numerical solutions. A key characteristic of the GITT is its hybrid numerical-analytical feature. As opposed to other numerical methods that attempt to solve the governing PDEs, our proposed solution for the concentration field requires solving an ODE system, which reduces the numerical effort. Also, since there are many ODE solvers available, our solution has a lower implementation effort than development of coupled PDE solver. Due to the analytical features of our solution, it is straightforward to derive the temporal evolution of the spatial moments of the concentration field. The proposed GITT solution can also be employed as a benchmark tool to validate existing numerical solutions. In a

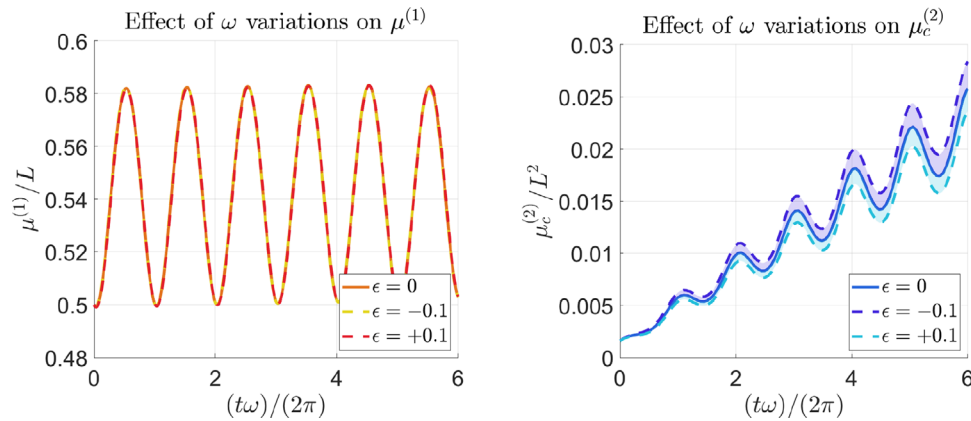


FIGURE 10 Temporal evolution of the first (left) and second central (right) spatial moments of the solute plume for different ω . All results displayed in dimensionless form

future extension of this work, we plan to consider transport through transversely isotropic media^{54,55} that show different mechanical and flow behaviors along and across the bedding plane.

This paper also presents the sensitivity of key transport metrics to selected geomechanical parameters such as c_m and S_k for the Terzaghi problem. Our results show that geomechanical properties can affect transport both at the global (i.e., spatial moments of the solute plume) and at the local scale (i.e., resident concentration). We note that the sensitivity of the solute concentration to the selected geomechanics parameters becomes even more relevant at late times, when a 20% variation in the chosen parameter can cause a 5% variation in the solute plume's peak concentration. This result shows the importance of accounting for geomechanical deformations in risk analysis that, in general, consists of estimating the peak concentration.⁵⁶ Our analysis highlights the importance of allocating resources toward improved characterization of geomechanical parameters, such as S_k and c_m , which are often times neglected in hydrological analysis. Finally, the results for the case of periodic load, which is representative of dynamic stress transfer from earthquakes, tides, or seasonal water level variations, reveal that ω has an impact on the concentration signal, especially at early times. On the other hand, the relative importance of ω will depend on the considered location where the concentration signal is being investigated. While varying ω does not affect the first moment of the solute plume, it seems to have an impact on the second central moment, enhancing the spreading of the solute for lower angular frequencies. This indicates that coupling between transport and geomechanical processes can contribute to enhanced solute mixing after earthquakes or other time-dependent loads.

ACKNOWLEDGMENTS

The first and last authors gratefully acknowledge the financial support by the National Science Foundation under Grant Number 1654009. The first author acknowledges partial support from the Annenberg PhD Fellowship.


CONFLICT OF INTEREST

The authors declare that they have no conflicts of interest.

ORCID

Alessandra Bonazzi  <https://orcid.org/0000-0002-6220-2164>

Birendra Jha  <https://orcid.org/0000-0003-3855-1441>

Felipe P. J. de Barros  <https://orcid.org/0000-0001-9104-0160>

REFERENCES

1. Yerkes RF, Castle RO. Seismicity and faulting attributable to fluid extraction. *Eng Geol.* 1976;10(2-4):151-167.
2. Segall P. Earthquakes triggered by fluid extraction. *Geology.* 1989;17(10):942-946.
3. Gambolati G, Teatini P. Geomechanics of subsurface water withdrawal and injection. *Water Resour Res.* 2015;51(6):3922-3955.
4. Galloway DL, Burbey TJ. Regional land subsidence accompanying groundwater extraction. *Hydrogeol J.* 2011;19(8):1459-1486.
5. Fialko Y, Simons M. Deformation and seismicity in the Coso Geothermal Area, Inyo County, California: observations and modeling using satellite radar interferometry. *J Geophys Res Solid Earth.* 2000;105(B9):21781-21793.

6. Ellsworth WL. Injection-induced earthquakes. *Science*. 2013;341(6142):1225942.
7. Keranen KM, Savage HM, Abers GA, Cochran ES. Potentially induced earthquakes in Oklahoma, USA: links between wastewater injection and the 2011 mw 5.7 earthquake sequence. *Geology*. 2013;41(6):699-702.
8. Morris JP, Hao Y, Foxall W, McNab W. A study of injection-induced mechanical deformation at the In Salah CO₂ storage project. *Int J Greenhouse Gas Control*. 2011;5(7):270-280.
9. Birkholzer JT, Zhou Q. Basin-scale hydrogeologic impacts of CO₂ storage: capacity and regulatory implications. *Int J Greenhouse Gas Control*. 2009;3(6):745-756.
10. Zhao X, Jha B. Role of well operations and multiphase geomechanics in controlling fault stability during CO₂ storage and enhanced oil recovery. *J Geophys Res Solid Earth*. 2019;124:6359-6375.
11. Biot MA. General theory of three-dimensional consolidation. *J Appl Phys*. 1941;12(2):155-164.
12. Geertsma J. A basic theory of subsidence due to reservoir compaction: the homogeneous case. *Verhandelingen Kon Ned Geol Mijnbouwk Gen*. 1973;28:43-62.
13. Gambolati G, Freeze RA. Mathematical simulation of the subsidence of venice: 1. Theory. *Water Resour Res*. 1973;9(3):721-733.
14. Bear J, Corapcioglu MY. Mathematical model for regional land subsidence due to pumping: 1. Integrated aquifer subsidence equations based on vertical displacement only. *Water Resour Res*. 1981;17(4):937-946.
15. Galloway DL, Hudnut KW, Ingebritsen S, et al. Detection of aquifer system compaction and land subsidence using interferometric synthetic aperture radar, Antelope Valley, Mojave Desert, California. *Water Resour Res*. 1998;34(10):2573-2585.
16. Gambolati G, Teatini P, Baù D, Ferronato M. Importance of poroelastic coupling in dynamically active aquifers of the Po River Basin, Italy. *Water Resour Res*. 2000;36(9):2443-2459.
17. Jha B, Juanes R. Coupled multiphase flow and poromechanics: a computational model of pore pressure effects on fault slip and earthquake triggering. *Water Resour Res*. 2014;50(5):3776-3808.
18. Roeloffs E. Poroelastic techniques in the study of earthquake-related hydrologic phenomena. In: Dmowska R, Saltzman B, eds. *Advances in Geophysics*. Vol. 37. New York: Elsevier; 1996:135-195.
19. Sneed M, Galloway DL, Cunningham WL. *Earthquakes: Rattling the Earth's Plumbing System*. Reston, VA: US Department of the Interior, US Geological Survey; 2003.
20. Montgomery DR, Manga M. Streamflow and water well responses to earthquakes. *Science*. 2003;300(5628):2047-2049.
21. Esteller M, Rodríguez R, Cardona A, Padilla-Sánchez L. Evaluation of hydrochemical changes due to intensive aquifer exploitation: case studies from Mexico. *Environ Monit Assess*. 2012;184(9):5725-5741.
22. Erban LE, Gorelick SM, Zebker HA, Fendorf S. Release of arsenic to deep groundwater in the Mekong Delta, Vietnam, linked to pumping-induced land subsidence. *Proc Natl Acad Sci*. 2013;110(34):13751-13756.
23. Fox PJ, Lee J, Lenhart JJ. Coupled consolidation and contaminant transport in compressible porous media. *Int J Geomech*. 2011;11(2):113-123.
24. Lewis T, Pivonka P, Fityus S, Smith D. Parametric sensitivity analysis of coupled mechanical consolidation and contaminant transport through clay barriers. *Comput Geotech*. 2009;36(1-2):31-40.
25. Hernández-Espriú A, Reyna-Gutiérrez JA, Sánchez-León E, et al. The drastic-sg model: an extension to the drastic approach for mapping groundwater vulnerability in aquifers subject to differential land subsidence, with application to Mexico City. *Hydrogeol J*. 2014;22(6):1469-1485.
26. Frigo M, Ferronato M, Yu J, et al. A parametric numerical analysis of factors controlling ground ruptures caused by groundwater pumping. *Water Resour Res*. 2019;55(1):9500-9518.
27. Ye S, Franceschini A, Zhang Y, et al. A novel approach to model earth fissure caused by extensive aquifer exploitation and its application to the Wuxi Case, China. *Water Resour Res*. 2018;54(3):2249-2269.
28. Yu X, Michael HA. Offshore pumping impacts onshore groundwater resources and land subsidence. *Geophys Res Lett*. 2019;46(5):2553-2562.
29. Lewis T, Pivonka P, Smith D. Theoretical investigation of the effects of consolidation on contaminant transport through clay barriers. *Int J Numer Anal Methods Geomech*. 2009;33(1):95-116.
30. Zhang H, Jeng DS, Barry DA, Seymour BR, Li L. Solute transport in nearly saturated porous media under landfill clay liners: a finite deformation approach. *J Hydrol*. 2013;479:189-199.
31. Zhang H, Jeng DS, Seymour B, Barry DA, Li L. Solute transport in partially-saturated deformable porous media: application to a landfill clay liner. *Adv Water Res*. 2012;40:1-10.
32. Tran M, Jha B. Coupling between transport and geomechanics affects spreading and mixing during viscous fingering in deformable aquifers. *Adv Water Res*. 2020;136:103485.
33. Li YC, Cleall PJ. Analytical solutions for advective-dispersive solute transport in double-layered finite porous media. *Int J Numer Anal Methods Geomech*. 2011;35(4):438-460.
34. Xie H, Yan H, Feng S, Wang Q, Chen P. An analytical model for contaminant transport in landfill composite liners considering coupled effect of consolidation, diffusion, and degradation. *Environ Sci Pollut Res*. 2016;23(19):19362-19375.
35. Cotta RM. *Integral Transforms in Computational Heat and Fluid Flow*. Boca Raton, FL: CRC Press; 1993.
36. de Barros FPJ, Cotta RM. Integral transforms for three-dimensional steady turbulent dispersion in rivers and channels. *Appl Math Modell*. 2007;31(12):2719-2732.
37. Cotta RM, Knupp DC, Naveira-Cotta CP, Sphaier LA, Quaresma JN. Unified integral transforms algorithm for solving multidimensional nonlinear convection-diffusion problems. *Numer Heat Transfer Part A Appl*. 2013;63(11):840-866.

38. Gutierrez MS, Lewis RW. Coupling of fluid flow and deformation in underground formations. *J Eng Mech.* 2002;128(7):779-787.
39. Wang HF. *Theory of Linear Poroelasticity with Applications to Geomechanics and Hydrogeology.* Princeton, NJ: Princeton University Press; 2017.
40. Peters GP, Smith DW. Solute transport through a deforming porous medium. *Int J Numer Anal Methods Geomech.* 2002;26(7):683-717.
41. Cheng AHD. *Poroelasticity.* Vol. 27. Berlin: Springer; 2016.
42. Karim M, Nogami T, Wang J. Analysis of transient response of saturated porous elastic soil under cyclic loading using element-free Galerkin method. *Int J Solids Struct.* 2002;39(24):6011-6033.
43. Raubenheimer B, Elgar S, Guza R. Estimating wave heights from pressure measured in sand bed. *J Waterway Port Coastal Ocean Eng.* 1998;124(3):151-154.
44. Michallet H, Mory M, Piedra-Cueva I. Wave-induced pore pressure measurements near a coastal structure. *J Geophys Res Oceans.* 2009;114(C6).
45. Elkhoury JE, Brodsky EE, Agnew DC. Seismic waves increase permeability. *Nature.* 2006;441(7097):1135-1138.
46. de Barros FPJ, Mills WB, Cotta RM. Integral transform solution of a two-dimensional model for contaminant dispersion in rivers and channels with spatially variable coefficients. *Environ Model Softw.* 2006;21(5):699-709.
47. Rubol S, Battiatto I, de Barros FPJ. Vertical dispersion in vegetated shear flows. *Water Resour Res.* 2016;52(10):8066-8080.
48. Mikhailov MD, Ozisik MN. *Unified Analysis and Solutions of Heat and Mass Diffusion.* New York: Dover; 1994.
49. Scheidegger AE. General theory of dispersion in porous media. *J Geophys Res.* 1961;66(10):3273-3278.
50. Hahn DW, Özisik MN. *Heat Conduction.* Hoboken, NJ: John Wiley & Sons; 2012.
51. Wolfram S. *The MATHEMATICA® Book, Version 4.* Cambridge: Cambridge University Press; 1999.
52. Fox PJ, Lee J, Lenhart JJ. Coupled consolidation and contaminant transport in compressible porous media. *Int J Geomech.* 2011;11(2):113-123.
53. Dentz M, Carrera J. Effective dispersion in temporally fluctuating flow through a heterogeneous medium. *Phys Rev E.* 2003;68(3):036310.
54. Zhang Q, Choo J, Borja RI. On the preferential flow patterns induced by transverse isotropy and non-Darcy flow in double porosity media. *Comput Meth Appl Mech Eng.* 2019;353:570-592.
55. Zhao Y, Borja RI. A continuum framework for coupled solid deformation–fluid flow through anisotropic elastoplastic porous media. *Comput Meth Appl Mech Eng.* 2020;369:113225.
56. Boso F, de Barros FPJ, Fiori A, Bellin A. Performance analysis of statistical spatial measures for contaminant plume characterization toward risk-based decision making. *Water Resour Res.* 2013;49(6):3119-3132.

How to cite this article: Bonazzi A, Jha B, de Barros FPJ. Transport analysis in deformable porous media through integral transforms. *Int J Numer Anal Methods Geomech.* 2020;1–18. <https://doi.org/10.1002/nag.3150>

APPENDIX A: DISCUSSION ON POROSITY

Let the Eulerian or “true” porosity at time t be defined as $\phi(t) = \frac{V_p(t)}{V_b(t)}$, where V_p and V_b are the pore and bulk volumes. The mass balance equation for the solid component of the porous body is

$$\frac{\partial[(1 - \phi)\rho_s]}{\partial t} + \nabla \cdot [(1 - \phi)\rho_s \mathbf{v}_s] = 0, \quad (\text{A.1})$$

where ρ_s is the solid density and \mathbf{v}_s is the solid skeleton velocity defined as the time rate of change of displacement. Applying the chain rule and dividing by ρ_s yields

$$\frac{1 - \phi}{\rho_s} \frac{\partial \rho_s}{\partial t} - \frac{\partial \phi}{\partial t} + \frac{1 - \phi}{\rho_s} \nabla \rho_s \cdot \mathbf{v}_s + \nabla \cdot [(1 - \phi)\mathbf{v}_s] = 0. \quad (\text{A.2})$$

The change in volume of the solid grains of the porous medium, which is subject to the change in total stress $\Delta\sigma_v$ and pressure change Δp , is the sum of two parts: the change due to Δp acting on $(1 - \phi)V_b$ and the change due to $\Delta\sigma_v + \Delta p$ acting on V_b , both with a compressibility given by $1/K_s$. This gives us the constitutive relation for ρ_s as a function of σ_v and p , which can be differentiated in time,

$$\frac{1}{\rho_s} \frac{\partial \rho_s}{\partial t} = -\frac{1}{K_s} \frac{1}{(1 - \phi)} \left(\frac{\partial \sigma_v}{\partial t} + \phi \frac{\partial p}{\partial t} \right). \quad (\text{A.3})$$

Substitute Equation (A.3) in (A.2), using the effective stress principle, $\sigma_v = K_{dr}\varepsilon_v - bp$, where K_{dr} is the drained bulk modulus related to K_v , and neglecting the product of the solid density gradient and the solid skeleton velocity, which is small for geomaterials, we obtain:

$$-\frac{d\phi}{dt} - \frac{K_{dr}}{K_s} \frac{\partial \varepsilon_v}{\partial t} + \frac{b - \phi}{K_s} \frac{\partial p}{\partial t} + (1 - \phi) \nabla \cdot \mathbf{v}_s = 0, \quad (\text{A.4})$$

where $\frac{d\phi}{dt} = \frac{\partial \phi}{\partial t} + \nabla \phi \cdot \mathbf{v}_s$ has been used. Since $\nabla \cdot \mathbf{v}_s = \partial \varepsilon_v / \partial t$ and $b = 1 - (K_{dr}/K_s)$, we obtain

$$\frac{d\phi}{dt} = (b - \phi) \frac{\partial \varepsilon_v}{\partial t} + \frac{b - \phi}{K_s} \frac{\partial p}{\partial t}, \quad (\text{A.5})$$

which can be integrated in time to yield,

$$\phi = b - (b - \phi_0) \exp(-\varepsilon_v - \Delta p/K_s). \quad (\text{A.6})$$

When the exponential term is expanded in an infinite series and all second- and higher-order terms are dropped, the above equation reduces to

$$\Delta \phi = \phi - \phi_0 = (b - \phi_0) \varepsilon_v + \frac{b - \phi_0}{K_s} \Delta p. \quad (\text{A.7})$$

This shows that changes in porosity must be small,³² eg, $\Delta \phi \sim \mathcal{O}(10^{-2})$ because the solid modulus is much larger than the typical change in pressure encountered during subsurface flow, $K_s \sim \mathcal{O}(10^{10})$ Pa and $\Delta p_{\max} \sim \mathcal{O}(10^6)$ Pa, and, from the infinitesimal strain definition of ε , $\varepsilon_v \sim \mathcal{O}(10^{-2})$. Equation (A.7) is analogous to Equation(28) in Ref. [17] for small changes in porosity. The Eulerian ADE under coupled flow and geomechanics is

$$\frac{\partial(\phi c)}{\partial t} + \nabla \cdot (\mathbf{q}c - \phi D \nabla c) = 0 \quad (\text{A.8})$$

which is Equation (16) written for a 3D domain. Applying the chain rule we obtain

$$\phi \frac{\partial c}{\partial t} + \nabla \cdot (\mathbf{q}c) - \phi D \nabla^2 c = D \nabla \phi \cdot \nabla c - c \frac{\partial \phi}{\partial t}, \quad (\text{A.9})$$

which shows the spatial and temporal fluctuations of porosity as source terms for the transport process.³² Neglecting these fluctuations, as justified above, we obtain the ADE of Equation (21).

APPENDIX B: DERIVATION OF THE SYSTEM OF COUPLED ODEs

Assuming a constant porosity $\phi(x, t) = \phi$, the ADE becomes:

$$\frac{\partial c(x, t)}{\partial t} + \frac{\partial(u(x, t)c(x, t))}{\partial x} = \frac{\partial}{\partial x} \left[D(x, t) \frac{\partial c(x, t)}{\partial x} \right], \quad (\text{B.1})$$

where $u(x, t) = q(x, t)/\phi$. Multiplying the ADE by $\Psi_i(x)$ and integrating in space leads to:

$$\begin{aligned} & \int_0^L \Psi_i(x) \frac{\partial c(x, t)}{\partial t} dx + \int_0^L \Psi_i(x) c(x, t) \frac{\partial u(x, t)}{\partial x} dx + \int_0^L \Psi_i(x) u(x, t) \frac{\partial c(x, t)}{\partial x} dx \\ &= \int_0^L \Psi_i(x) D_0 \frac{\partial^2 c(x, t)}{\partial x^2} dx + \int_0^L \Psi_i(x) \frac{\partial \check{D}(x, t)}{\partial x} \frac{\partial c(x, t)}{\partial x} dx + \int_0^L \Psi_i(x) \check{D}(x, t) \frac{\partial^2 c(x, t)}{\partial x^2} dx. \end{aligned} \quad (\text{B.2})$$

Using Equation (22), the first term in Equation (B.2) is given by:

$$\int_0^L \tilde{\Psi}_i(x) \frac{\partial c(x,t)}{\partial t} dx = \frac{\partial}{\partial t} \int_0^L \tilde{\Psi}_i(x) c(x,t) dx = \frac{\partial \hat{c}_i(t)}{\partial t}. \quad (\text{B.3})$$

The second term in Equation (B.2) can be computed as:

$$\int_0^L \tilde{\Psi}_i(x) c(x,t) \frac{\partial u(x,t)}{\partial x} dx = \int_0^L \tilde{\Psi}_i(x) \frac{\partial u(x,t)}{\partial x} \left(\sum_{j=0}^{\infty} \tilde{\Psi}_j(x) \hat{c}_j(t) \right) dx = \sum_{j=0}^{\infty} \hat{c}_j(t) U_{ij}(t), \quad (\text{B.4})$$

where

$$U_{ij}(t) = \int_0^L \tilde{\Psi}_i(x) \frac{\partial u(x,t)}{\partial x} \tilde{\Psi}_j(x) dx. \quad (\text{B.5})$$

As for the third term in Equation (B.2), we use Equation (23) to obtain:

$$\int_0^L \tilde{\Psi}_i(x) u(x,t) \frac{\partial c(x,t)}{\partial x} dx = \int_0^L u(x,t) \tilde{\Psi}_i(x) \frac{\partial}{\partial x} \left(\sum_{j=0}^{\infty} \tilde{\Psi}_j(x) \hat{c}_j(t) \right) dx = \sum_{j=0}^{\infty} \hat{c}_j(t) A_{ij}(t), \quad (\text{B.6})$$

where

$$A_{ij}(t) = \int_0^L u(x,t) \tilde{\Psi}_i(x) \frac{\partial \tilde{\Psi}_j(x)}{\partial x} dx. \quad (\text{B.7})$$

The fourth term of Equation (B.2) is evaluated using integration by parts in conjunction with the boundary conditions in Equations (18)–(19), (26)–(27), and (25):

$$\int_0^L \tilde{\Psi}_i(x) D_0 \frac{\partial^2 c(x,t)}{\partial x^2} dx = D_0 \int_0^L c(x,t) \frac{\partial^2 \tilde{\Psi}_i(x)}{\partial x^2} dx = -\zeta^2 \hat{c}_i(t). \quad (\text{B.8})$$

As for the last two terms in Equation (B.2), we integrate by parts and apply the boundary conditions in Equations (18)–(19):

$$\int_0^L \tilde{\Psi}_i(x) \frac{\partial \check{D}(x,t)}{\partial x} \frac{\partial c(x,t)}{\partial x} + \int_0^L \tilde{\Psi}_i(x) \check{D}(x,t) \frac{\partial^2 c(x,t)}{\partial x^2} = - \int_0^L \check{D}(x,t) \frac{\partial \tilde{\Psi}_i(x)}{\partial x} \frac{\partial c(x,t)}{\partial x} dx. \quad (\text{B.9})$$

Applying the inverse from Equation (23), we have:

$$- \int_0^L \check{D}(x,t) \frac{\partial \tilde{\Psi}_i(x)}{\partial x} \frac{\partial}{\partial x} \left(\sum_{j=0}^{\infty} \tilde{\Psi}_j(x) \hat{c}_j(t) \right) dx = - \sum_{j=0}^{\infty} \hat{c}_j(t) B_{ij}(t), \quad (\text{B.10})$$

where

$$B_{ij}(t) = \int_0^L \check{D}(x,t) \frac{\partial \tilde{\Psi}_i(x)}{\partial x} \frac{\partial \tilde{\Psi}_j(x)}{\partial x} dx. \quad (\text{B.11})$$

Therefore, Equation (B.2) becomes:

$$\frac{d\hat{c}_i(t)}{dt} = - \sum_{j=0}^{\infty} \hat{c}_j(t) U_{ij}(t) - \sum_{j=0}^{\infty} \hat{c}_j(t) A_{ij}(t) - \zeta^2 \hat{c}_i(t) - \sum_{j=0}^{\infty} \hat{c}_j(t) B_{ij}(t), \quad (\text{B.12})$$

where $U_{ij}(t)$, $A_{ij}(t)$, and $B_{ij}(t)$ are defined in Equations (B.5), (B.7) and (B.11). To solve the equation, we also need an initial condition, which is provided by the integral transform of the initial condition in Equation (20):

$$\hat{c}_i(0) = \int_0^L \tilde{\Psi}_i(x) \frac{e^{-\frac{(x-\mu_c)^2}{2\sigma_c^2}}}{\sqrt{2\pi\sigma_c}} dx. \quad (\text{B.13})$$

APPENDIX C: SOLUTION FOR A VARIABLE POROSITY

Similar to Appendix B, we provide steps necessary to derive the coupled system of ODEs for the case of a variable porosity, which is relevant for soft or loosely consolidated rocks that are highly stress-sensitive. Multiplying Equation (21) for $\tilde{\Psi}(x)$ and integrating over the domain, we obtain:

$$\begin{aligned} & \int_0^L \tilde{\Psi}_i(x) \phi(x, t) \frac{\partial c(x, t)}{\partial t} dx + \int_0^L \tilde{\Psi}_i(x) c(x, t) \frac{\partial q(x, t)}{\partial x} dx + \int_0^L \tilde{\Psi}_i(x) q(x, t) \frac{\partial c(x, t)}{\partial x} dx \\ &= \int_0^L \tilde{\Psi}_i(x) \phi(x, t) D_0 \frac{\partial^2 c(x, t)}{\partial x^2} dx + \int_0^L \tilde{\Psi}_i(x) \phi(x, t) \check{D}(x, t) \frac{\partial^2 c(x, t)}{\partial x^2} dx \\ &+ \int_0^L \tilde{\Psi}_i(x) D_0 \frac{\partial \phi(x, t)}{\partial x} \frac{\partial c(x, t)}{\partial x} dx + \int_0^L \tilde{\Psi}_i(x) \frac{\partial c(x, t)}{\partial x} \frac{\partial}{\partial x} (\check{D}(x, t) \phi(x, t)) dx, \end{aligned} \quad (\text{C.1})$$

defining for simplicity a function:

$$F(x, t) = \phi(x, t) \check{D}(x, t). \quad (\text{C.2})$$

Performing all the integrations and using the boundary conditions defined in Equations (18)–(19) and (26)–(27), we obtain:

$$\sum_{j=0}^{\infty} \frac{d\hat{c}_j(t)}{dt} P_{ij}(t) = - \sum_{j=0}^{\infty} \hat{c}_j(t) Q_{ij}(t) - \sum_{j=0}^{\infty} \hat{c}_j(t) R_{ij}(t) - D_0 \sum_{j=0}^{\infty} \hat{c}_j(t) M_{ij}(t) - \sum_{j=0}^{\infty} \hat{c}_j(t) W_{ij}(t), \quad (\text{C.3})$$

where the only unknown is the term $\hat{c}_i(t)$. In Equation (C.3), we have:

$$\begin{aligned} P_{ij}(t) &= \int_0^L \tilde{\Psi}_i(x) \phi(x, t) \tilde{\Psi}_j(x) dx; & Q_{ij}(t) &= \int_0^L \tilde{\Psi}_i(x) \frac{\partial q(x, t)}{\partial x} \tilde{\Psi}_j(x) dx; \\ R_{ij}(t) &= \int_0^L q(x, t) \tilde{\Psi}_i(x) \frac{\partial \tilde{\Psi}_j(x)}{\partial x} dx; & M_{ij}(t) &= \int_0^L \phi(x, t) \frac{\partial \tilde{\Psi}_i(x)}{\partial x} \frac{\partial \tilde{\Psi}_j(x)}{\partial x} dx; \\ W_{ij}(t) &= \int_0^L F(x, t) \frac{\partial \tilde{\Psi}_i(x)}{\partial x} \frac{\partial \tilde{\Psi}_j(x)}{\partial x} dx. \end{aligned} \quad (\text{C.4})$$